

# Robust B-spline Snakes For Ultrasound Image Segmentation

Clovis Tauber · Hadj Batatia · Alain Ayache

Received: 28 December 2007 / Revised: 14 March 2008 / Accepted: 4 April 2008 / Published online: 17 May 2008  
© 2008 Springer Science + Business Media, LLC. Manufactured in The United States

**Abstract** Snake-based methods are commonly used to segment ultrasound images. However, their performance is generally limited because of the specific properties of this kind of images. This paper addresses the sensitivity of parametric active contours to speckle within ultrasound images. We propose a new B-spline snake model, founded on two original external energies specifically tailored for the segmentation of biomedical speckled images. First, the curve is attracted from a wide capture range with an expansion energy that facilitates the snake initialization. Then, it is accurately fitted on the region boundaries with an energy that allows precise positioning of the curve along edges in ultrasound images. A mutual inhibition function is designed to control the two energies. Results on real ultrasound images are presented and quantitatively compared to the boundaries manually outlined by experts. Our method improves the precision of heart cavities segmentation.

**Keywords** B-spline snakes · Biomedical imaging · Segmentation · Speckle · Ultrasound images

## 1 Introduction

Image segmentation techniques require increased robustness, better reliability and high automation. This is especially the case for biomedical image processing.

Imaging techniques such as ultrasound, X-ray computed tomography and magnetic resonance imaging are now ubiquitous in hospitals. This paper addresses ultrasound imagery, which is the most used technique. Such images are characterized by echoes dropouts, low contrast and speckle contamination. The speckle is a multiplicative, locally correlated noise caused by the destructive interference of signals reflected from scatterers within one resolution cell. This phenomenon degrades the quality of images and makes difficult the detection of their features. Ultrasound image segmentation is therefore traditionally considered more difficult than segmenting incoherent images.

Variational methods, and more precisely active contours [13], have been used to solve image segmentation problems. These methods adopt either edge based or region based approaches.

Among edge based methods, Caselles et al. [3] proposed geodesic active contours, where the problem of minimizing the energy functional is transformed into a problem of geodesic computation in a Riemannian space, according to a new metric. Leventon et al. [14] imposed a shape prior to the level set function, introduced by Malladi et al. [17], during the segmentation process. The resulting shape prior was shown to strongly improve segmentation results obtained on 2D and 3D biomedical images. Delingette et al. [7] introduced an energy which attracts the curve towards high curvature contour points, aiming at a better segmentation of irregular contours. Ziplock snakes were proposed by Neuenschwander et al. [18]. Their external energy first affects their extremities; then, the influence moves towards the center of the open snake. Davatzikos and Prince used the ribbon snakes in the context of cortex segmentation [6].

---

C. Tauber (✉) · H. Batatia · A. Ayache  
IRIT-ENSEEIH, 2 rue Camichel BP7122,  
31071 Toulouse cedex 7, France  
e-mail: tauber@enseeiht.fr

The regions of an image may have some properties that cannot be represented by a contour integral. In opposition to edge based active contours, whose evolution is controlled by edges, the evolution of region based active contours is controlled by characteristics of regions. Ronfard [22] proposed one of the first region based active contours. This method uses the Ward distance and a heuristic method to control the evolution of the curve. Chan et al. proposed an active contour without edges, based on the region statistics of inside and outside the closed curve [4]. Jehan-Besson et al. [12] used a hybrid external energy, based on edges and regions. They established the first evolution equation using derivatives of region descriptors.

Most of these variational methods rely on the intensity gradient to compute the external energies. However, considering an edge as the maximum of the first derivative of intensity is not appropriate in ultrasound imaging due to the multiplicative nature of speckle.

This work addresses two major limitations of the explicit variational methods for ultrasound image segmentation: their sensitivity to speckle and to the precision of the initialization. We propose an original variational method based on two complementary external forces. A fitting force precisely positions the curve along the contours in speckled images, while an expansion force greatly increases the catching range of the fitting force, to reduce the sensitivity to initialization. The mutual influence of the corresponding forces is controlled with an inhibition factor.

The remainder of this paper is organized as follows. First, we present in Section 2 the coefficient of variation and show that it can be used as an edge detector in speckled images. Section 3 describes the two new external energies and the proposed robust B-spline snake (RBS). Results on real ultrasound images are presented in Section 4, and quantitatively compared with manual outlines from experts. Finally, Section 5 draws some conclusions.

## 2 Coefficient of Variation Analysis

### 2.1 Global and Local Versions

Imaging speckle is a phenomenon which occurs when a coherent source and an incoherent detector are used to interrogate a medium which is rough on the scale of the wavelength. The most widely used techniques to reduce speckle in synthetic aperture radar imaging include the filters of Lee, Frost, Kuan and the Gamma Maximum a Posteriori ([15, 16] and references therein).

These methods all rely on the coefficient of variation to characterize the speckle. There are two types of coefficients of variation (CV): the global coefficient of variation, denoted  $\mathcal{G}$  and the local coefficient of variation, denoted  $\gamma$ .

The global CV is defined as:

$$\mathcal{G}^2 = \frac{\text{var}(I)}{\bar{I}^2} \quad (1)$$

where  $\text{var}(I)$  and  $\bar{I}$  are the variance and the mean of the intensity of an area having a homogeneous reflectivity. The local coefficient of variation  $\gamma$  is a local version of the global CV, defined as:

$$\gamma^2(s) = \frac{1}{|\eta_s|} \sum_{p \in \eta_s} \frac{(I_p - \bar{I}_s)^2}{\bar{I}_s^2} \quad (2)$$

where  $\eta_s$  is a neighborhood of a central pixel  $s$ .  $\bar{I}_s$  is the mean intensity of  $\eta_s$ . In this paper we consider that  $\eta_s$  is a  $3 \times 3$  square window.

### 2.2 Properties of the Coefficient of Variation

The coefficient of variation has the following properties:

*Property 1: The global coefficient of variation characterizes the level of speckle in the image.*

Let  $R$  be the reflectivity of an observed scene,  $I$  the actual observation and  $n$  a multiplicative noise:

$$I(i, j) = R(i, j) \cdot n(i, j) \quad (3)$$

The global CV is calculated in an  $N$ -pixel area  $\Omega_h$  of homogeneous reflectivity:

$$\forall (i, j) \in \Omega_h, R(i, j) = k. \quad (4)$$

Thus, the global CV can be written as:

$$\mathcal{G}_{\Omega_h} = \frac{\frac{1}{N} \sum_{(i,j) \in \Omega_h} (kn(i, j) - k\bar{n})^2}{(k\bar{n})^2} = \frac{\text{var}(n)}{\bar{n}^2}.$$

This shows that the global CV does not depend on the reflectivity of the considered area; it only depends on the multiplicative noise. Hence, it characterizes the speckle affecting the image.

*Property 2: The coefficient of variation is an edge detector robust to the speckle.*

The variance of a variable  $A$  can be written as:

$$\text{var}(A) = E(A^2) - E(A)^2 \quad (5)$$

It is reasonable to consider that the real reflectivity of a scene and the speckle affecting it are independent.

As a consequence, the equation of the local CV can be written:

$$\gamma = \frac{\text{var}(Rn)}{E(Rn)^2} \tag{6}$$

$$= \frac{1}{E(Rn)^2} [E((Rn)^2) - E(Rn)^2] \tag{7}$$

$$= \frac{1}{E(Rn)^2} [( \text{var}(R) + E(R)^2 ) \cdot ( \text{var}(n) + E(n)^2 ) - E(R)^2 E(n)^2] \tag{8}$$

$$= \underbrace{\frac{\text{var}(n) E(R)^2}{E(Rn)^2}}_{\text{global CV}} + \text{var}(R) \frac{( \text{var}(n) + E(n)^2 )}{E(Rn)^2} \tag{9}$$

As the mean is the best approximation of the expectation defined for a finite set of equiprobable pixels, the first term of Eq. 9 corresponds to the global CV. The second term is positive, increasing with the variance of the real reflectivity. This shows that  $\gamma$  is close to  $\mathcal{G}$  within homogeneous regions, and largely greater than  $\mathcal{G}$  on edges. Therefore, the coefficient of variation can effectively be used as an edge detector for images affected by speckle.

### 2.3 Comparison Between the Coefficient of Variation and the Gradient of Intensity

Most research work on edge-based segmentation of medical images is based on the gradient of intensity when measuring the appartenance of pixels to contours.

Although effective for additive noise, this measure is inappropriate for images affected by speckle. Figure 1 illustrates this statement. The gradient of intensity and the local CV are calculated on two speckled images (Fig. 1b and 1f). The first features a single homogeneous region and the second composes of two distinct homogeneous regions separated by a sharp edge.

Figure 1a and 1d show that the variance of the gradient of intensity increases with the intensity in homogeneous regions. This expected behaviour is due to the multiplicative nature of speckle. The local CV features a different property; it has more homogeneous values (Fig. 1c and 1f). As a consequence, the edge of the second image (Fig. 1e) is clearly more precisely detectable with the local CV than it is with the gradient of intensity. The very high values of the gradient within the bright region can incorrectly be identified as edges.

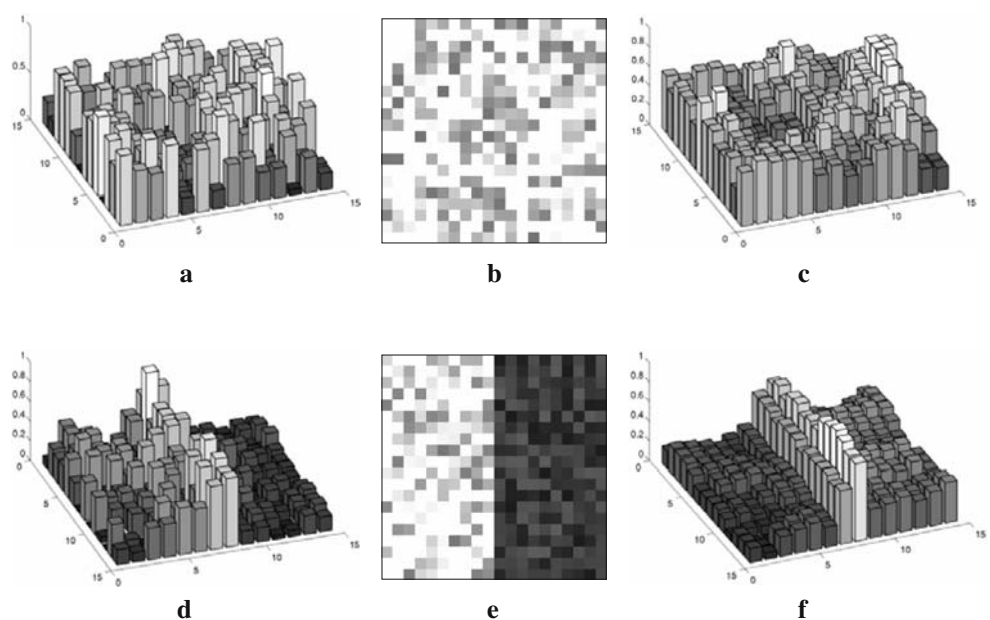
Aiming at precise ultrasound image segmentation, we thus conclude that the two external energies of our B-spline snake model should be based on the coefficient of variation rather than the conventional gradient of intensity.

## 3 Robust B-spline Snakes

### 3.1 B-splines in the Context of Snakes

A snake is a curve that evolves from an initial position towards the boundary of an object, minimizing some energy functional [5, 13, 25]. Such functional consists of two terms: the internal energy and the external energy.

**Figure 1** Comparison of the gradient of intensity and local CV when detecting edges in speckled images. **a** Normalized gradient of intensity of image **b**. **b** Speckled homogeneous image. **c** Normalized local coefficient of variation of image **b**. **d** Normalized gradient of intensity of image **e**. **e** Speckled image with contour. **f** Normalized local coefficient of variation of image **e**.



The first term affects the smoothness of the curve, while the second attracts the snake towards image features. Splines can be effectively integrated in the snakes model, as they can characterize a continuous parametric curve by a vector of control points [21, 24]. The benefit of using splines comes from the implicit properties of the model, including the local support and the control of the continuity of the curve.

The functional defining the energy of a B-spline having the equation  $s(u) = (x(u), y(u))$  is [13]:

$$E_{\text{snake}} = E_{\text{intern}}(s(u)) + E_{\text{extern}}(s(u)) \quad (10)$$

The following sections present the energies that define the B-spline snake model that we developed.

### 3.2 Parameterization and Internal Energy

The B-spline snake parameterization is the function which associate each node  $p_i$  with a parameter  $u_i$ . The nodes are the junctions between the parts of the interpolating spline.

To be effective, a parameterization has to be as close as possible to the nodes geometry [9]. It can be seen as the time spent on an interval. The parameterization is uniform when  $\forall i, u_{i+1} = u_i + k$ , without considering the relative distance between two consecutive nodes along the curve. A brutal spacing change between two nodes diminishes the geometrical continuity of the curve. To avoid this, some methods consider the distance between the nodes to define the parameterization [10].

Brigger et al. [2] demonstrated that cubic B-splines with knots on the integer are optimal to minimize the functional defined by Kass and Witkin [13]. However, when the curvature is compared with the second derivative of the curve, they make the implicit supposition that the spline has to be parameterized by the curvilinear abscissa.

In our method, we adopt this curvilinear abscissa parameterization. To maintain it during the snake evolution, this either implies to:

- recompute the parameter of each node at every iteration;
- keep constant the parameters and reposition the nodes along the curve at each iteration.

The second solution is more cost-effective. We adopt a constant and uniform parameterization:  $u_i = i$ .

First, nodes are uniformly spaced on the initial curve. This parameterization then necessitates checking the nodes disposition at each iteration and maintaining their regular spacing. We embed this node positioning within the B-spline snake internal energy.

The internal energy reaches its minimum when the nodes are uniformly distributed along the curve. Let  $M$  be the number of nodes and  $e_m$  the mean difference of curvilinear abscissa between two nodes:

$$e_m = \frac{1}{M} \int_0^M (x'(u)^2 + y'(u)^2)^{\frac{1}{2}} du \quad (11)$$

$e_m$  matches the speed  $s'(u)$  of  $s(u)$  when it is parametrized with the curvilinear abscissa. The established internal energy is written [11]:

$$E_{\text{intern}} = \oint ||s'(u)|^2 - e_m^2|^2 du. \quad (12)$$

When the snake evolves under this constraint, the nodes evolve tangently to the curve towards a regular spacing. This ensures that the parameterization remains close to the curvilinear abscissa parameterization.

To maintain the desired geometric continuity, we avoid fixing the number of nodes. We define  $\Lambda$  as the rigidity parameter of our model. It indicates the required length between two consecutive nodes. At each iteration, the mean space  $e_m$  between consecutive nodes is compared to two thresholds: an upper threshold  $\Lambda_{\text{high}} = \Lambda + \frac{\Lambda}{M}$  and a lower threshold  $\Lambda_{\text{low}} = \Lambda - \frac{\Lambda}{M}$ . If the distance is high ( $e_m > \Lambda_{\text{high}}$ ), a node is added on the longest segment of the curve to increase the flexibility. Inversely, if the distance is low ( $e_m < \Lambda_{\text{low}}$ ), a node is removed on the shortest segment to smooth the snake.

### 3.3 Fitting External Energy

First, we filter the image with a speckle adapted anisotropic diffusion [23]. After the diffusion process, we compute a local CV contours map as:

$$I_\gamma(i, j) = \begin{cases} \gamma(i, j) & \text{if } \gamma(i, j) > \mathcal{G}, \\ 0 & \text{otherwise.} \end{cases} \quad (13)$$

where  $\mathcal{G}$  is the global CV of the image resulting from the diffusion, and  $\gamma(i, j)$  is the local CV at pixel  $(i, j)$  of the same image. Figure 2 illustrates the result of the diffusion on an ultrasound image and its corresponding edge map.

As shown in Section 2, the coefficient of variation characterizes the speckle and can be used to differentiate homogeneous regions from contours. Similarly to some external energies based on the intensity gradient [11, 19], we construct a fitting energy that both considers the amplitude of the gradient of the local CV and its direction ( $\vec{\nabla} I_\gamma$ ), which is perpendicular to the contour (Fig. 3).

We establish our external fitting energy as:

$$E_{\text{extern}}(s(u)) = - \left[ \vec{\nabla} I_\gamma(s(u)) \cdot (\vec{n}(s(u))) \right] \quad (14)$$

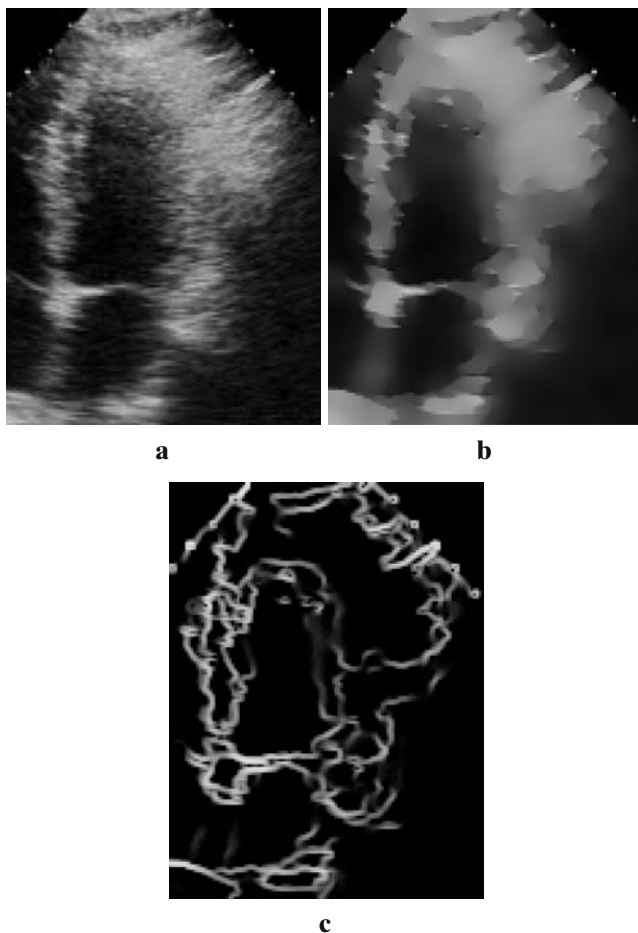


**Figure 2** Ultrasound image and the corresponding local CV contour map. **a** Initial image. **b** Anisotropic diffusion result. **c** Local CV contour map.

where  $\vec{n}(s(u))$  is the normal unit vector to the B-spline snake  $s$ .

Figure 3 shows the amplitude of the external energy for a given vector  $\vec{\nabla}I_\gamma$  and its angle  $\theta$  with  $\vec{n}$  the normal unit vector to the curve.

To compute the proposed energy, the curve is sampled between the nodes. This energy is called *fitting external energy* as it leads to precise positioning of the curve along the boundaries in images affected by speckle.

However, despite its precision, this energy has a limited range; it is therefore insufficient when the initial curve is far from the contours. To address this problem, we propose an additional energy called expansion energy.

### 3.4 Expansion External Energy

Traditional active contours do not have large capture range due to the rapid decrease of external forces with the distance from the contour. In order to obtain an

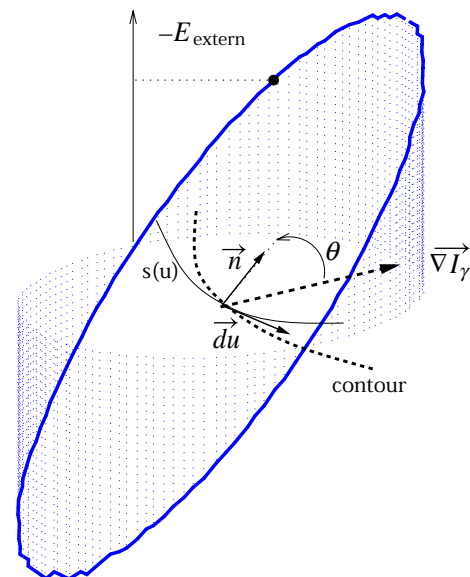


**Figure 3** External energy of the B-snake varying with the angle between  $\vec{n}$  and  $\vec{\nabla}I_\gamma$ .

acceptable solution, the initial contour generally has to be close to the desired contour. Some approaches have been proposed to solve this initialization problem. Cohen introduced the balloon snakes [5], in which a pressure force is added to the interior of the curve, considering the snake as an inflated balloon. It partially solves the drawback of false local minima caused by random edges. However, it introduces an additional parameter which controls the balance between overpassing local extrema and stopping on actual edges. Xu et al. [25] propose the gradient vector flow (GVF). The GVF is computed as the diffusion of the gradient vectors of a gray level image. This external force for snakes permits flexible initialization, reducing its effects on the final result. However, it is less effective in presence of speckle as it is controlled by the intensity gradient.

Our additional external energy, called thereafter *expansion energy* and denoted s-GVF for Speckle-resistant GVF, allows the detection of discontinuous and subjective contours, as well as a more flexible initialization in ultrasound images. It is a GVF [25] model that attracts the snake towards pixels having high coefficient of variation.

The value of this energy is based on the thresholded local CV map,  $I_\gamma$ , where the gradients  $\vec{\nabla}I_\gamma$  of pixels located on a contour are perpendicular to its direction. The amplitude of  $\vec{\nabla}I_\gamma$  is high on the contours, and decreases rapidly as the curve moves further. It becomes zero inside homogeneous regions, where  $I_\gamma(x, y) = 0$ . Hence, under the lone influence of the fitting external energy, the curve is guided towards a precise contour segmentation but requires a very close initialization.

The s-GVF, calculated from the local coefficient of variation, solves this problem and prevents the snake from overpassing the contours in speckled images. It is, consequently, more robust than the classical GVF for ultrasound image segmentation.

The s-GVF,  $\mathbf{v}(x, y) = [u(x, y), v(x, y)]$ , is the vector flow that minimizes the functional:

$$\mathcal{E} = \iint \mu(u_x^2 + u_y^2 + v_x^2 + v_y^2) + |\overrightarrow{\nabla I_\gamma}|^2 |\mathbf{v} - \overrightarrow{\nabla I_\gamma}|^2 dx dy. \tag{15}$$

where  $\mu$  is a regulation parameter. In homogeneous regions, the amplitude of  $|\overrightarrow{\nabla I_\gamma}|$  is low and the second term is neglected. The functional is therefore dominated by the sum of the square partial derivatives of the s-GVF (Eq. 15). This results in slow variations of the field in homogeneous regions. When  $|\overrightarrow{\nabla I_\gamma}|$  is predominant (i.e. on the contours), the local CV gradient vector field is the solution that minimizes the functional  $\mathcal{E}$ :  $\mathbf{v} = \overrightarrow{\nabla I_\gamma}$ . To sum up, the s-GVF is a field of vectors varying slowly and pointing towards the nearest edge in  $I_\gamma$ . The resolution is performed using the Euler equations:

$$\mu \nabla^2 u - \left( u - \frac{\partial I_\gamma}{\partial x} \right) \left( \frac{\partial I_\gamma^2}{\partial x} + \frac{\partial I_\gamma^2}{\partial y} \right) = 0 \tag{16}$$

$$\mu \nabla^2 v - \left( v - \frac{\partial I_\gamma}{\partial y} \right) \left( \frac{\partial I_\gamma^2}{\partial x} + \frac{\partial I_\gamma^2}{\partial y} \right) = 0. \tag{17}$$

### 3.5 Sequencing the Expansion and Fitting Energies

The expansion force is used to initialize the curve and expand it towards the boundaries, whereas the fitting energy is used to position the curve along the contours, but has a short range. Therefore, the two energies have to be sequenced to increase precision and avoid overlapping. The sequencing is done by progressively reducing the expansion term while the snake gets closer to the contours. The amplitudes of the s-GVF vectors are modified with a function that we call the *inhibition factor*, defined as follows.

First, we define a coarse map  $\mathcal{R}$  of the distances to the contour:

$$\mathcal{R}(p = (i, j)) = \min_{q \in I_\gamma^+} \|p - q\| \tag{18}$$

where  $I_\gamma^+$  is the set of pixels in  $I_\gamma$  with non zero intensity.

The inhibition factor is constructed from the weighting function of Tukey. The matrix of inhibition factors is calculated as:

$$\Xi(i, j) = \begin{cases} \frac{3\mathcal{R}(i, j)^2}{\zeta^2} - \frac{3\mathcal{R}(i, j)^4}{\zeta^4} + \frac{\mathcal{R}(i, j)^6}{\zeta^6} & \text{if } \mathcal{R}(i, j) \leq \zeta, \\ 1 & \text{otherwise.} \end{cases} \tag{19}$$

where  $\zeta$  is the inhibition parameter that determines the distance above which the s-GVF is not inhibited. When  $\mathcal{R}(i, j) < \zeta$ , the inhibition factor  $\Xi(i, j) < 1$ .

The normalized s-GVF at  $(i, j)$  is:

$$\mathbf{v}_N(i, j) = \frac{\mathbf{v}(i, j)}{\sqrt{|u(i, j)|^2 + |v(i, j)|^2}} \tag{20}$$

We use the inhibition factor as a weight on the s-GVF amplitude. The weighted s-GVF, noted  $\mathbf{v}_{Ni}(i, j)$  is calculated as:

$$\mathbf{v}_{Ni}(i, j) = \mathbf{v}_N(i, j) \cdot \Xi(i, j). \tag{21}$$

### 3.6 Curve Evolution

The energy functional formulation of the s-GVF produces external force fields that can be expected to have both irrotational and solenoidal components [25]. The s-GVF is therefore not entirely irrotational, as are the traditional snake potential fields. Due to the solenoidal component of the s-GVF, the corresponding external force cannot be calculated as the opposite gradient of a potential function. Therefore we consider the curve evolution as a four-step iterative process:

1. update the number of nodes according to the curve length and the parameter  $\Lambda$ ;
2. perform a gradient descent step on the global energy;
3. make nodes evolve within the inhibited s-GVF field;
4. update the global snake energy and calculate the size of the next gradient descent step.

The global energy of the snake is defined as:

$$E_{global} = \alpha E_{intern} + (1 - \alpha) E_{fitting}. \tag{22}$$

The stopping criterion is based on the variation of the global energy and the length of the snake. This is because within homogeneous regions, the snake energy can be stationary while its length growth.

### 4 Experimentations

We compare here the results of our algorithm with those of Jacob et al. [11] and Xu et al. [25] using two ultrasound images. The method of Jacob et al. relies on an hybrid external energy based on both the gradient of intensity and region based information. In Tables 1 and 2,  $Jacob_{init1}$ ,  $Jacob_{init2}$  and  $Jacob_{init3}$  are three results corresponding to three initial curves of increasing precision,  $Jacob_{init3}$  being related to a very precise initialization. The initialization having lesser impact on the method of Xu et al., we present the results for several values of the rigidity parameter.  $Xu_{rigid1}$  corresponds to no rigidity.  $Xu_{rigid2}$  corresponds to a rigidity parameter equal to the external energy weight. Finally, the rigidity used for  $Xu_{rigid3}$  is the strongest (ten times the external energy weight).

The proposed B-spline snake, called RBS, has also been experimented with different parameter values of  $\Lambda$ .

Manual outlines of doctors are used as ground truth to compare the results. When curves are displayed on an image, the dynamic range of the intensity of the initial image is mapped onto  $[[0, 127]]$  for better results visualization.

#### 4.1 Quantitative Evaluation Techniques

To validate our model, we calculated several indicators of performance which we briefly describe here. The calculus of these indicators is always related to the ground truth established by doctors. We denote  $C_{seg}$  the resulting curve of a variational segmentation method and  $A_{seg}$  the area delimited by  $C_{seg}$ . We denote

**Table 1** Quantitative results for the segmentation of ultrasound image from Fig. 4a: ASM, AC, SSM and MHD.

Method	ASM	AC (%)	SSM	MHD (pixels)
$Xu_{rigid1}$	0.7592	63.43	0.4070	4.0279
$Xu_{rigid2}$	0.7817	55.84	0.4691	3.4993
$Xu_{rigid3}$	0.8516	31.34	0.4782	3.4823
$Jacob_{init1}$	0.6555	-46.03	0.5372	9.3636
$Jacob_{init2}$	0.7809	-14.53	0.5950	4.9867
$Jacob_{init3}$	0.8921	24.19	0.6592	2.1659
$RBS_{\Lambda=3}$	0.9561	2.94	0.7253	1.3235
$RBS_{\Lambda=5}$	0.9774	-1.52	0.7305	1.3003
$RBS_{\Lambda=10}$	0.9780	-1.48	0.7591	1.0902
$RBS_{\Lambda=15}$	0.9177	-11.34	0.7777	1.3116
$RBS_{\Lambda=17}$	0.9252	-9.52	0.7274	1.4370

**Table 2** Quantitative results for the segmentation of ultrasound image from Fig. 7a: ASM, AC, SSM and MHD.

Method	ASM	AC (%)	SSM	MHD (pixels)
$Xu_{rigid1}$	0.9366	13.54	0.5706	3.0700
$Xu_{rigid2}$	0.9419	12.34	0.5620	3.1026
$Xu_{rigid3}$	0.9395	12.89	0.5969	3.0052
$Jacob_{init1}$	0.8493	-31.03	0.2846	14.1001
$Jacob_{init2}$	0.9365	-4.40	0.3776	4.9932
$Jacob_{init3}$	0.9559	9.23	0.5496	2.7731
$RBS_{\Lambda=5}$	0.9743	1.74	0.6957	1.7901
$RBS_{\Lambda=10}$	0.9798	1.66	0.6644	1.9579
$RBS_{\Lambda=20}$	0.9814	1.64	0.6895	1.8773

$C_{doctor}$  the contour manually delineated by a doctor and  $A_{doctor}$  the area delimited by  $C_{doctor}$ .

- Area Similarity Measure (ASM): this measure was introduced by Zijdenbos, and used in [20]. The ASM between two segmentation results  $A_{seg}$  and  $A_{doctor}$  is a float  $S \in [0, 1]$  which is defined as:

$$S = \frac{2card(A_{seg} \cap A_{doctor})}{card(A_{seg}) + card(A_{doctor})} \tag{23}$$

This measure is sensitive to the size of the compared regions and to their relative position. A value close to 1 indicates a good area similarity.

- Area comparison (AC): the AC indicates how strongly the algorithm under (or over) estimates the size of the region of interest. It is a percentage defined as:

$$AC = \frac{card(A_{seg}) - card(A_{doctor})}{\min\{card(A_{seg}), card(A_{doctor})\}} \tag{24}$$

- Shape Similarity Measure (SSM): while the ASM is an interesting measure of the relative size and position of the segmented regions, it is less precise to measure the similarity of shapes. SSM, introduced by Pluempitwiriyawej et al. [20], is derived from the correspondence method of Chamfer [1]. The SSM measure can be written:

$$S_{SSM} = \frac{1}{card(C_{seg})} \sum_{(x,y) \in C_{seg}} \Gamma_r(x, y) S_{phase}(x, y) \tag{25}$$

where  $S_{phase}$  is the phase similarity. The term  $\Gamma_r$  is used to lower the phase similarity when corresponding pixels are far from each other. It includes a parameter to weight the similarity of localisation.

- Modified Hausdorff distance (MHD): this was introduced by Dubuisson et al. [8]:

$$\mathcal{H}(C_{seg}, C_{doctor}) = \max(h_{mod}(C_{seg}, C_{doctor}), h_{mod}(C_{doctor}, C_{seg})) \tag{26}$$

with  $h$  the modified oriented distance of Hausdorff (Figs. 4, 5, and 6):

$$h_{\text{mod}}(\mathcal{C}_{\text{seg}}, \mathcal{C}_{\text{doctor}}) = \frac{1}{\text{card}(\mathcal{C}_{\text{seg}})} \sum_{a \in \mathcal{C}_{\text{seg}}} \min_{b \in \mathcal{C}_{\text{doctor}}} \|a - b\| \quad (27)$$

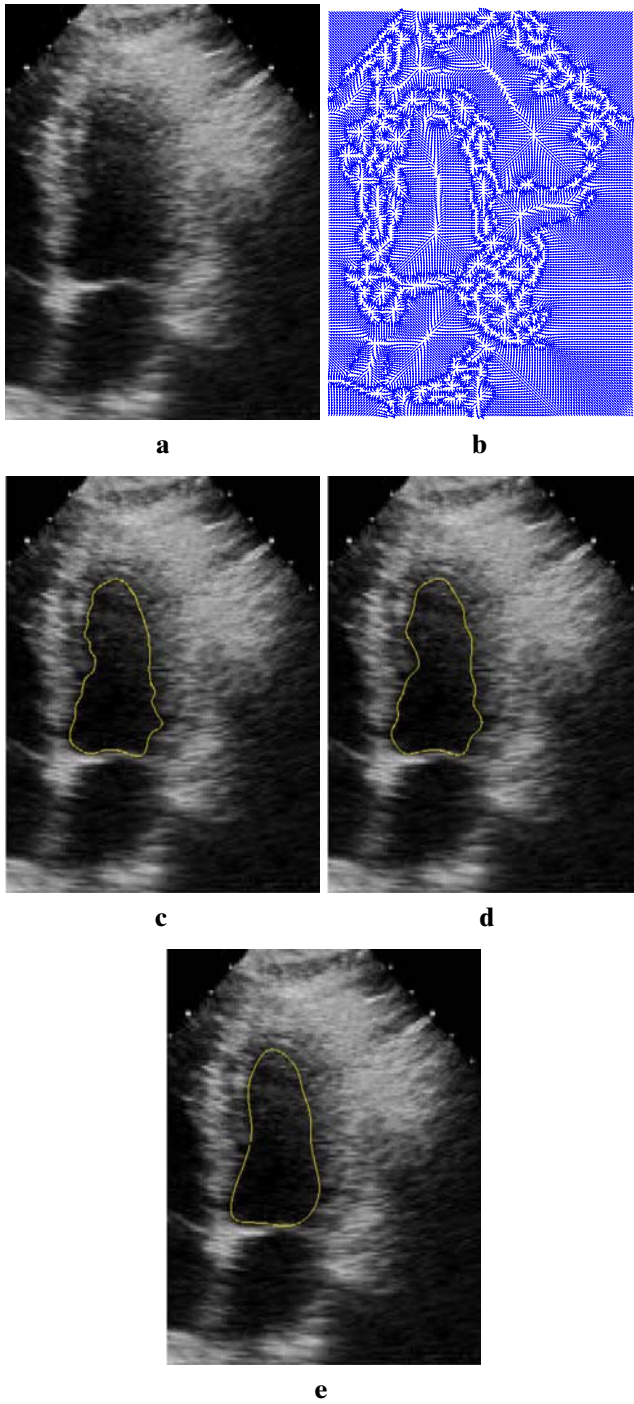


**Figure 4** RBS segmentation results on an ultrasound image. **a** Initial image. **b** s-GVF. **c**  $\text{RBS}_{\Lambda=5}$ . **d**  $\text{RBS}_{\Lambda=10}$ . **e**  $\text{RBS}_{\Lambda=15}$ .

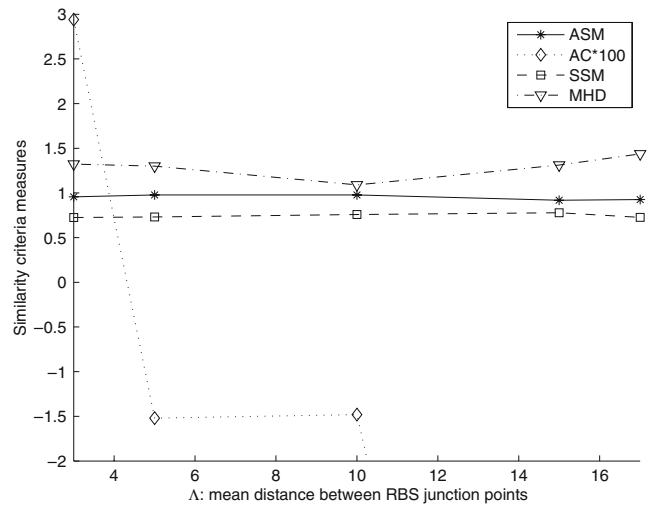


**Figure 5** Criteria evolution with mean node spacing  $\Lambda$  of the RBS for segmentation of image (Fig. 4a).

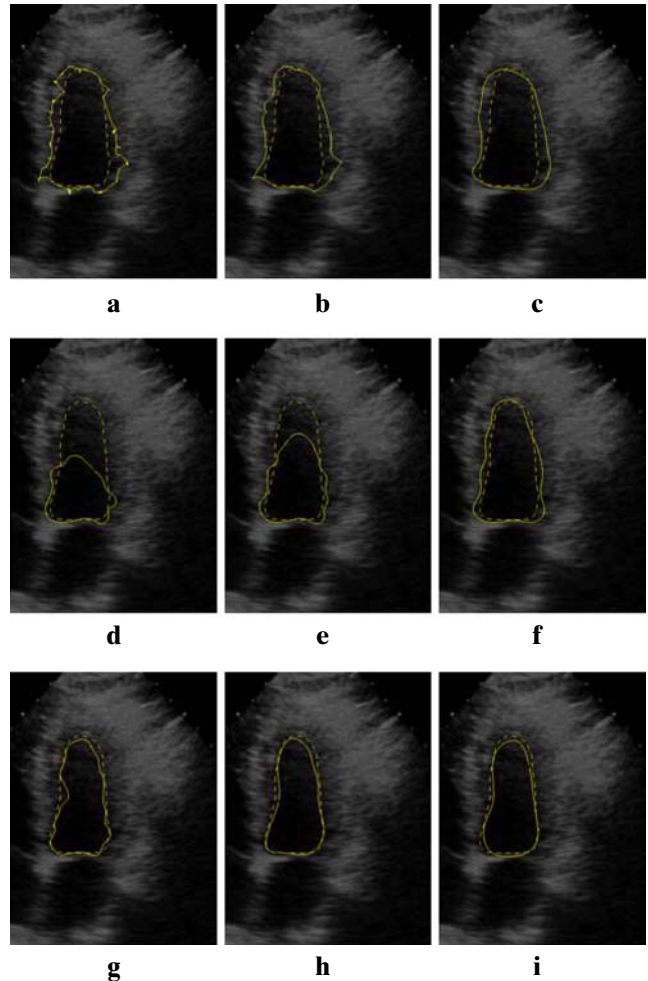


**Figure 6** Comparison of Jacob et al., Xu et al. and RBS methods on image (Fig. 4a) with the doctors outline. **a**  $\text{Xu}_{\text{rigid}1}$ . **b**  $\text{Xu}_{\text{rigid}2}$ . **c**  $\text{Xu}_{\text{rigid}3}$ . **d**  $\text{Jacob}_{\text{init}1}$ . **e**  $\text{Jacob}_{\text{init}2}$ . **f**  $\text{Jacob}_{\text{init}3}$ . **g**  $\text{RBS}_{\Lambda=5}$ . **h**  $\text{RBS}_{\Lambda=10}$ . **i**  $\text{RBS}_{\Lambda=15}$ .

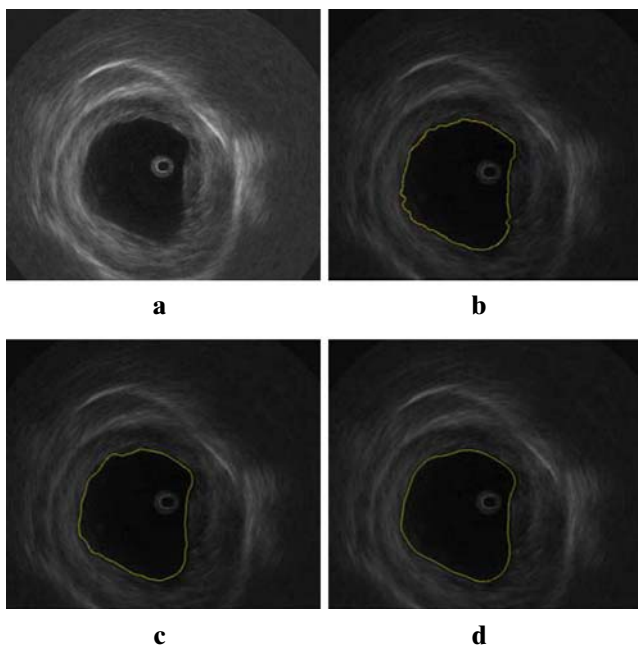


**Figure 7** RBS segmentation results on an ultrasound image. **a** Initial image. **b**  $RBS_{\Lambda=5}$ . **c**  $RBS_{\Lambda=10}$ . **d**  $RBS_{\Lambda=20}$ .

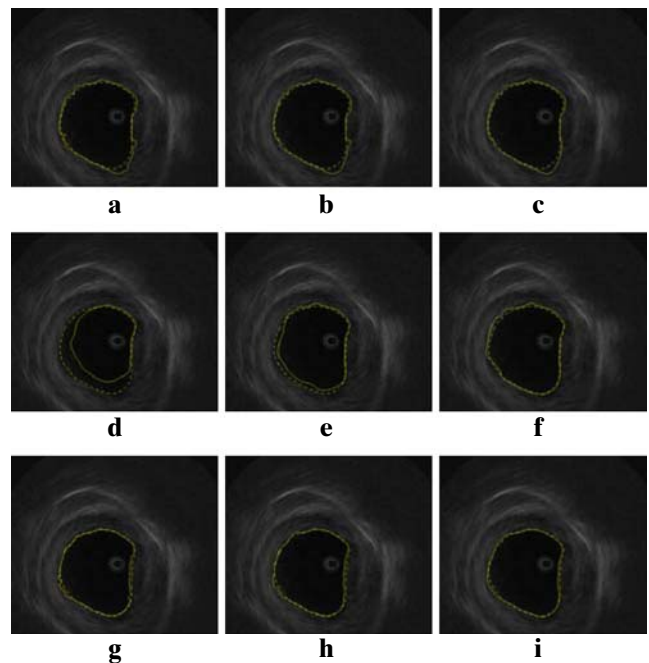


**Figure 9** Comparison of Jacob et al., Xu et al. and RBS methods on image (Fig. 7a) with the doctors outline.

### 4.2 Result Analysis

An overview of the quantitative results is presented in Tables 1 and 2. For both ultrasound images, the RBS scores are better than those of other parametric active contours. We note in Table 2 the globally high values of the ASM for all segmentation methods on image (Fig. 7a). This was predictable as the higher ultrasound frequency used to acquire the image makes it easier to segment than the first one, due to the higher resolution. Figures 6 and 9 present the results

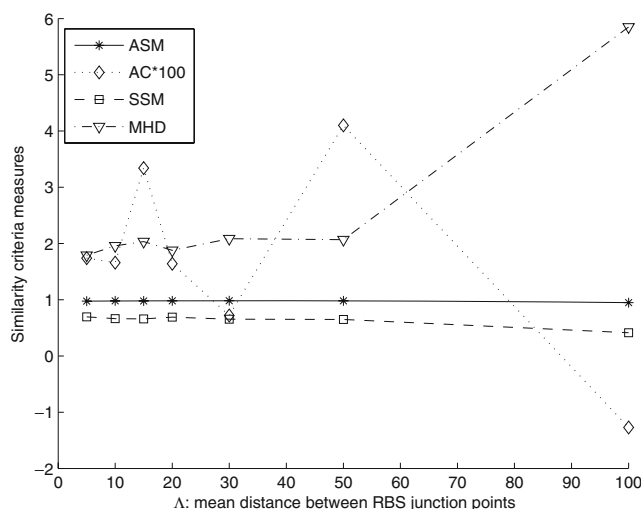


**Figure 8** Criteria evolution with mean node spacing  $\Lambda$  of the RBS for segmentation of image (Fig. 7a).

compared with the manual outlines of the doctors. The results of all methods (Jacob, Xu or RBS) appear in continuous line while the manual outline of the doctor is dashed. Xu and Jacob results predictably suffer the relative imprecision of the gradient of intensity in ultrasound images, compared to the coefficient of variation. Our RBS method leads to the most precise results, for different values of  $\Lambda$ . In both case, the heart cavities detection is close to the manual delineation by the doctors.

Finally, Figs. 5 and 8 show the influence of the parameter  $\Lambda$  on the quality of the RBS segmentation, illustrated in bottom rows of Figs. 6 and 9. The abscissa corresponds to the target mean distance  $\Lambda$  between two consecutive nodes, and the ordonate is without dimension. Criteria ASM and SSM are very stable, even for high values of  $\Lambda$ . MHD is stable but diverges from  $\Lambda = 50$  on the first image. Finally, the AC is the less stable among the four measures.

### 5 Discussion and Conclusions

In this paper we presented a new B-spline snake model for ultrasound image segmentation. The study of the geometric continuity of the snake has led to the internal energy choice justification. We proposed two original external energies based on the coefficient of variation. The first one precisely fits the snake on the region

of interest boundaries. The second one increases the attracting range of the external energy and facilitates the snake initialization. During the snake evolution, competition between the external energies is controlled by an inhibiting function that progressively lowers the expansion energy amplitude near the contours. The experimental results on real images confirmed that the construction of coefficient of variation based external energies improved the quality of the segmentation of heart cavities in ultrasound images. In the future, we plan to develop an hybrid active contour model with an additional region-based energy to take into account the local statistics of speckle in biomedical imaging.

## References

- Borgefors, G. (1988). Hierarchical chamfer matching: A parametric edge matching algorithm. *IEEE Transactions on Pattern Analysis And Machine Intelligence*, *10*, 849–865.
- Brigger, P., Hoeg, J., & Unser, M. (2000). B-spline snakes: A flexible tool for parametric contour detection. *IEEE Transactions on Image Processing*, *9*, 1484–1496.
- Caselles, V., Kimmel, R., & Sapiro, G. (1997). Geodesic active contours. *International Journal of Computer Vision*, *22*, 61–79.
- Chan, T., & Vese, L. (2001). Active contours without edges. *IEEE Transactions on Image Processing*, *10*(2), 266–277.
- Cohen, L. (1991). On active contour models and balloons. *Computer Vision, Graphics, And Image Processing: Image Understanding*, *53*, 211–218.
- Davatzikos, C., & Prince, J. L. (1995). An active contour model for mapping the cortex. *IEEE Transactions on Medical Imaging*, *14*, 65–80.
- Delingette, H., Hebert, M., & Ikeuchi, K. (1991). Shape representation and image segmentation using deformable surfaces. *Image and Vision Computing*, *10*(3), 132–144.
- Dubuisson, M. P., & Jain, A. K. (1994). A modified hausdorff distance for object matching. In *International conference on pattern recognition*. Jerusalem, Israel, October.
- Farin, G. (1992). *Curves and surfaces for computer-aided geometric design*. London: Academic.
- Foley, T. (1987). Interpolation with interval and point tension controls using cubic weighted  $v$ -spline. *ACM Transactions on Mathematical Software*, *13*, 68–96.
- Jacob, M., Blu, T., & Unser, M. (2004). Efficient energies and algorithms for parametric snakes. *IEEE Transactions on Image Processing*, *13*, 1231–1244.
- Jehan-Besson, S., Barlaud, M., & Aubert, G. (2003). DREAM2S: Deformable regions driven by eulerian accurate minimization method for image and video segmentation. *International Journal of Computer Vision*, *53*, 45–70.
- Kass, M., Witkin, A., & Terzopoulos, D. (1988). Snakes: Active contour models. *International Journal of Computer Vision*, *1*, 321–332.
- Leventon, M. E., Grimson, W. E. L., & Faugeras, O. (2000). Statistical shape influence in geodesic active contours. *Computer Vision and Pattern Recognition*, *1*, 316–323.
- Lopes, A., Touzi, R., Nezry, E. (1990). Adaptive speckle filters and scene heterogeneity. *IEEE Transactions on Geoscience and Remote Sensing*, *28*, 992–1000.
- Lopes, A., Nezry, E., Touzi, R., & Laur, H. (1993). Structure detection and statistical adaptive speckle filtering in SAR images. *International Journal of Remote Sensing*, *14*, 1735–1758.
- Malladi, R., Sethian, J. A., & Vemuri, B. C. (1995). Shape modeling with front propagation: A level set approach. *IEEE Transactions on Pattern Analysis and Machine Intelligence*, *17*, 158–174.
- Neuenschwander, W., Fua, P., Szekely, G., & Kubler, O. (1994). Making snakes converge from minimal initialization. *Conference ARPA Image Understanding Workshop*, *2*, 1627–1636.
- Park, H., Schoepflin, T., & Kim, Y. (2001). Active contour model with gradient directional information: Directional snake. *IEEE Transactions on Circuits and Systems for Video Technology*, *11*, 252–256.
- Pluempitwiriyaew, C., Moura, J., Wu, Y., & Ho, C. (2004). STACS: New active contour scheme for cardiac MR image segmentation. *IEEE Transactions on Medical Imaging*, *24*(5), 593–603.
- Precioso, F., Barlaud, M., Blu, T., & Unser, M. (2003). Smoothing b-spline active contour for fast and robust image and video segmentation. *Image Processing, 2003. Proceedings. 2003 International Conference on* (Vol. 1, pp. 37–40).
- Ronfard, R. (1996). Region-based strategies for active contour models. *International Journal of Computer Vision*, *13*, 229–251.
- Tauber, C., Batatia, H., & Ayache, A. (2004). A robust speckle reducing anisotropic diffusion. *Proceedings of IEEE international conference on image processing ICIP*.
- Unser, M. (1999). Splines: A perfect fit for signal and image processing. *IEEE Signal Processing Magazine*, *16*, 22–38.
- Xu, C., Prince, J. L. (1998). Snakes, shapes, and gradient vector flow. *IEEE Transactions on Image Processing*, *7*, 359–369.



**Clovis Tauber** received his PhD from the National Polytechnic Institute of Toulouse, France in Computer Science and Telecommunications in 2005. He had a Post-doctoral position at Institut de Recherche en Informatique de Toulouse (IRIT) from 2005 to 2007. He is currently a Post-doctoral research associate with Institut Pasteur in Paris. His scientific interests include biomedical signal and image processing, adaptive and nonlinear image processing, image filtering, segmentation and registration.



**Hadj Batatia** is a senior lecturer at the Institut National Polytechnique of Toulouse and researcher in the Institut de Recherche en Informatique de Toulouse. He received his Msc and PhD in computer engineering at Institut National polytechnique. He worked as senior lecturer in the university of Malaysia Sarawak from 1995 to 1997 and in the University of Teesside in the UK from 1997 to 1999. He is the head of the computer science department of CNAM in the region of Midi-Pyrenees. His research interests include statistical and variational models for medical image reconstruction, registration, filtering, and segmentation. His most recent work focused on cardiac

motion analysis using ultrasound images, modelling respiratory motions in PET lung images, and characterising skin optical tomography images.



**Alain Ayache** is the head of the Institute of Computer Science and Applied Mathematics of Toulouse (ENSEEIH). His research interests are biomedical image processing, learning styles and architectures, and axial stereovision.